

# Multipolarization Time Series of Sentinel-1 SAR Imagery to Analyze Variations of Reservoirs' Water Body

Emanuele Ferrentino<sup>ID</sup>, Student Member, IEEE, Ferdinando Nunziata<sup>ID</sup>, Senior Member, IEEE,  
Andrea Buono<sup>ID</sup>, Student Member, IEEE, Angelo Urciuoli<sup>ID</sup>, Student Member, IEEE,  
and Maurizio Migliaccio<sup>ID</sup>, Fellow, IEEE

**Abstract**—In this article, a two-year time-series of multipolarization Sentinel-1 synthetic aperture radar (SAR) imagery is exploited to analyze the changes in the water-covered area of the Monte Cotugno (Italy) reservoir. A two-step processing chain, which includes water/land separation and waterline extraction, is proposed to accomplish this task. Experimental results, verified using independent *in situ* measurements, demonstrate that: first, Sentinel-1 time series can be successfully used to support the smart water management of reservoirs. In fact, the changes in the water-covered area inferred from the SAR time series agree with the seasonal behavior and they also fit anomalies; and second, multipolarization feature outperforms single-polarization ones in terms of accuracy of the extracted waterline profile.

**Index Terms**—Polarimetry, reservoir monitoring, synthetic aperture radar (SAR), smart water management (SWM).

## I. INTRODUCTION

S MART water management (SWM) consists of using Information and Communication Technology (ICT) tools to provide automatic real-time information to assist the planning and the development of regional and/or national strategies for the management of water resources. SWM includes solutions for key environmental and socioeconomic issues, e.g., water quality, efficient irrigation, floods, droughts, etc. The main ICT infrastructure consists of sensors' networks, geographic information system and smart meters, whose outputs are integrated into a smart grid architecture that follows the so-called Internet of Things framework [1].

A key parameter when dealing with the real-time monitoring and management of water bodies is the extent of the water-covered area [2]. In this context, satellite remote sensing

Manuscript received May 10, 2019; revised October 31, 2019; accepted December 9, 2019. Date of publication January 22, 2019; date of current version March 2, 2019. This work was supported by the European Space Agency within the frame of ESA-MOST (Ministry of Science and Technology) Dragon 4 Cooperation (Microwave satellite measurements for coastal area and extreme weather monitor, Project ID 32235). (Corresponding author: Maurizio Migliaccio.)

The authors are with the Dipartimento di Ingegneria, Università degli Studi di Napoli Parthenope, Napoli 80133, Italy (e-mail: emanuele.ferrentino@uniparthenope.it; ferdinando.nunziata@uniparthenope.it; andrea.buono@uniparthenope.it; angelo.urciuoli@uniparthenope.it; maurizio.migliaccio@uniparthenope.it).

Color versions of one or more of the figures in this article are available online at <http://ieeexplore.ieee.org>.

Digital Object Identifier 10.1109/JSTARS.2019.2961563

represents a noncooperative tool that can be effectively used to improve/complement *in situ* sensors' and actuators' networks to implement an effective and efficient SWM system. In particular, the analysis of time series of satellite-based measurements can provide cost-effective and reliable information for the management of water reservoirs. The topic addressed in this article belongs to the more general problem of monitoring closed water basins to support the detection of early warning evidence of potential ecosystem issues [3]. In addition, information on water levels provides first-hand knowledge on the amount of available water. This is an important information for local and regional authorities [4].

Within this context, optical remote sensing is widely employed for a twofold reason: optical imagery is simple to be interpreted and allow a spatial and temporal sampling that is accurate enough for monitoring reservoirs [5], [6]. However, remotely sensed optical measurements are weather- and sun-dependent and, therefore, their operational use is limited to daylight and cloud-free conditions. These limitations can be overcome by using microwave active sensors that guarantee all-day and almost all-weather observations together with a wide area coverage [7]. Accordingly, the synthetic aperture radar (SAR), being an imaging radar characterized by moderate-to-fine spatial resolution, is a key tool to support the SWM, even though the image interpretability is not at all straightforward due to speckle noise and eventual limitations in water/land separability [8], [9].

To properly frame the proposed methodology, state-of-the-art approaches aimed at exploiting the SAR imagery to monitor the water extent of inland water basins are briefly summarized. In [2], dam displacements and reservoir water levels of the Castello dam on the Magazzolo reservoir are analyzed by visual matching and unsupervised classification techniques. Results, undertaken to combine the X-band SAR and optical imagery from different sources, show that optical and radar sensors carry on complementary information that can be exploited to improve land/water discrimination. In [3], image processing techniques are exploited to monitor the water-area variations of the Dongting Lake, China. Experiments, undertaken using a time series of Environmental Satellite Advanced SAR imagery, show that the SAR can effectively monitor changes in the water-basin extent. In [10], the same lake is monitored using co- and cross-polarized backscattering coefficients measured by Sentinel-1 SAR. An

empirically set threshold is used to distinguish water body from the surrounding environment. In [11], water bodies are detected in the Spiritwood buried valley using a method based on the Otsu algorithm. Experiments, undertaken using RadarSAT-2 quad-polarization imagery, show that the cross-polarized channel outperforms copolarized channels in terms of enhancement land/water contrast. In [12], histogram-based thresholding is applied to map the water body of the Poyang Lake (China), using Sentinel-1 single-polarization (SP) SAR imagery. Experimental results show that the dense sampling provided by Sentinel-1 satellites allow monitoring monthly variations of water bodies. In addition, significant variability of the Poyang lake waterbody is observed at both seasonal and interannual scales. In [13], Sentinel-1 dual-polarization (DP) SAR imagery is combined with LandSAT eight optical observations showing that the joint use of microwave and optical imagery provides a better understanding of the wetland seasonal dynamics of the Seyfe lake (Turkey). In [14], COSMO-SkyMed X-band SAR data, together with ground observations and numerical modeling, are shown to be a reliable tool to estimate the total infiltration capacity of the artificial recharge basin area of the Po plain (Italy).

In this article, a time series of multipolarization Sentinel-1 SAR data is used to support the SWM of reservoirs. A processing chain is developed to extract the waterline and estimate the extent of the water-covered area extent from dual-polarization VV-VH (vertical transmit and receive–vertical transmit and horizontal receive) Sentinel-1 SAR measurements in an unsupervised way. A multipolarization analysis is performed to analyze the performance of waterline extraction methods based on SP and DP SAR measurements. The proposed rationale is discussed using actual Sentinel-1 scenes collected over the Monte Cotugno reservoir, see Fig. 1, which is the largest embanked dam in Europe and one of the main civil infrastructures in Southern Italy, severely affected by seepage and leakage [15]. The methodology proposed to extract waterline from SAR scenes is contrasted with state-of-the-art methods and the water-area estimations are verified using independent *in situ* information on the Monte Cotugno reservoir available from its SWM system. Experimental results show that the DP approach outperforms SP one and the state-of-the-art method and the water area estimations well fit *in situ* observations being able to follow both seasonal trends and anomalies. The remainder of the article is organized as follows. In Section II, the methodology is described; while test site, data set, and experiments are shown and discussed in Section III. Conclusions are drawn in Section IV.

## II. METHODOLOGY

In this section, the methodology proposed to monitor the temporal evolution of the waterline using the DP SAR imagery is presented.

A DP SAR sensor provides partial polarimetric information, i.e. only co- and cross-polarized scattering amplitudes, namely  $S_{xx}$  and  $S_{xy}$ , where  $\{x, y\} \in \{H, V\}$  which are both exploited in the proposed methodology that can be focused into two steps: enhancement of water/land separability and edge detection method, see Fig. 2.

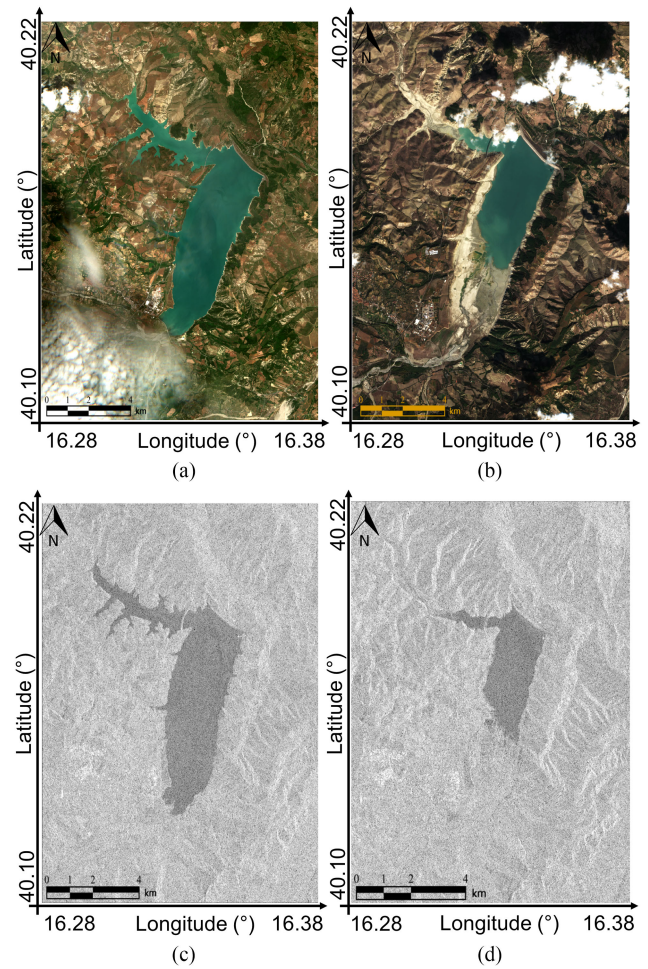


Fig. 1. (a) and (b) Excerpts of Sentinel-2 optical imagery collected over the test site area that includes the Monte Cotugno reservoir, when it is almost completely (June 12, 2016) partially (November 4, 2017) covered by water, respectively. (c) and (d) Corresponding excerpts of Sentinel-1 VV-polarized SAR imagery.

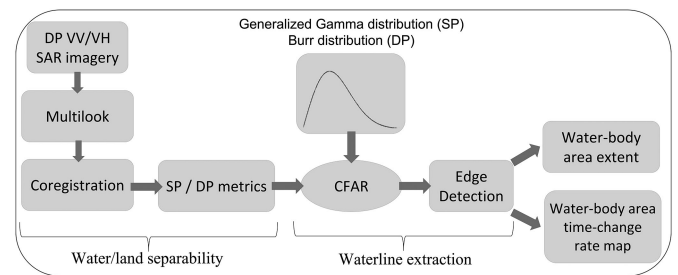


Fig. 2. Block diagram of the proposed approach. First step: water/land separability, performed using  $r$  (DP),  $\sigma_{VV}^0$  and  $\sigma_{VH}^0$  (SP); second step: combination of CFAR and edge detection to extract the waterline and generate added-value products.

The first step consists of preprocessing the SAR dataset. This step includes spatial multilooking to reduce the speckle noise, resampling to generate square-pixel images, and multitemporal coregistration of all the scenes.

The second step consists of extracting the waterline using both SP and DP channels. First, the waterline is extracted along the whole time series of Sentinel-1 SAR imagery and, then,

the extent of the water covered is estimated by using the pixels labeled as “water” in the binary image.

When dealing with waterline extraction, two tasks must be addressed. The first one aims at enhancing the land/water separation using a metric that depends on the polarimetric information content. When dealing with SP measurements, the normalized radar cross section (NRCS), which is proportional to the square modulus of the scattering amplitude, is exploited; when dealing with DP measurements, the available co- and cross-polarimetric channels are exploited. The second task consists of extracting the 1-pixel continuous waterline by applying an edge detector algorithm onto a binary image, where land and water are clearly distinguished. In this article, the edge detector based on the Sobel kernel, which measures the 2-D spatial gradient on the binary image to emphasize edges, is used since it provides the best tradeoff between the detection accuracy and time effectiveness [16].

When using dual-polarimetric channels to estimate waterline, different combinations of co- and cross-polarized channels can be adopted. In this article, the metric we adopted is based on the product of co- and cross-polarized amplitude channels:

$$r = \langle |S_{VV}| \cdot |S_{VH}| \rangle \quad (1)$$

where  $|\cdot|$  and  $\langle \cdot \rangle$  stand for modulus and spatial averaging, respectively. This metric was shown in [17]–[19] to maximize the land/sea contrast when dealing with coastline extraction. It is worth noting that  $r$ , which is related to the geometric mean, is complemented by the geometric ratio, i.e., the ratio between co- and cross-polarized scattering amplitude [20]. In this article, the geometric ratio is not used since we experimentally verified that it does not perform well in enhancing the land/sea contrast.

From a physical viewpoint,  $r$  is expected to enhance the land/water contrast with respect to the SP channel. In fact, the backscattering is expected to be dominated by Bragg/tilted Bragg or specular reflection according to the roughness of the water-covered area. In both cases, a low cross-polarized backscattering signal is expected that results in small  $r$  values. When dealing with land areas, due to the orography and the presence of vegetation, urban settlements, rocky areas, etc., a more complicated and, to some extent unpredictable, mixture of scattering mechanisms is generally expected that results in: 1) larger copolarized backscattering values due to the dielectric permittivity that is generally larger than water; 2) nonnegligible cross-polarized backscattering values due to depolarizing and/or repolarizing mechanisms related to the terrain tilting with respect to the sensor’s line-of-sight. Hence, larger  $r$  values are generally expected.

The waterline extraction method based on SP measurements consists of exploiting co- and cross-polarized channel information separately. In this article, the VV- and VH-polarized NRCSs are considered, namely  $\sigma_{VV}^0$  and  $\sigma_{VH}^0$ , respectively, which are given by

$$\sigma_{xy}^0 = \frac{4\pi}{k^2} |S_{xy}|^2 \quad (2)$$

where  $k$  is the electromagnetic wave number.

The second step consists of processing the metric  $r$  using a constant false alarm rate (CFAR) method to generate a binary

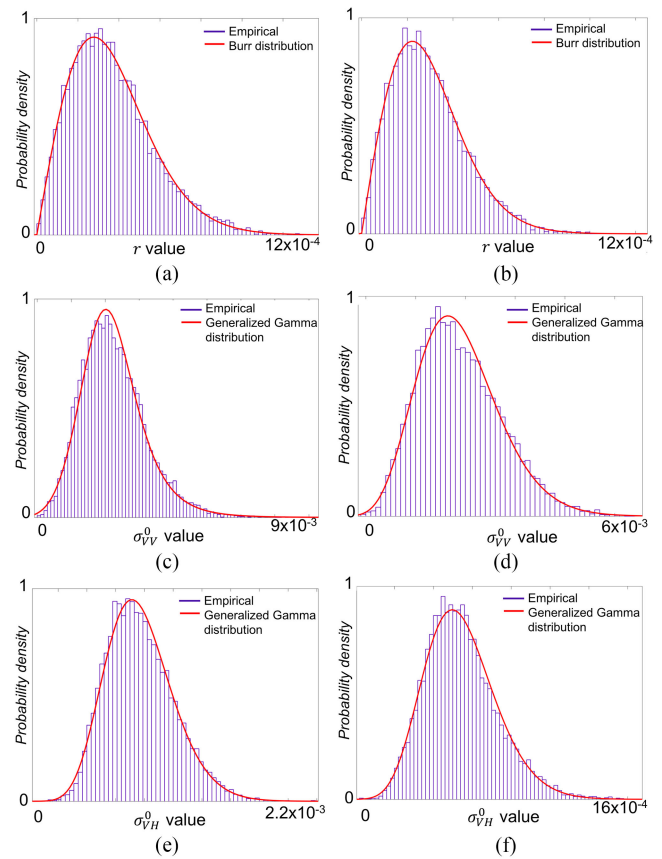


Fig. 3. Histograms evaluated within water-covered ROIs extracted from the SAR scenes shown in Fig. 1(c) and (d). Rows refer to the parameters  $r$  (a) and (b),  $\sigma_{VV}^0$  [(c)–(d)] and  $\sigma_{VH}^0$  (e) and (f), while columns refer to the SAR scenes. The corresponding best-fit theoretical pdfs, i.e., Burr in (a) and (b) and GGD in (c)–(f) are also shown in red.

image where the water-covered area can be clearly identified. To design a CFAR detector, the clutter statistical distribution must be analyzed. Hence, a region of interest (ROI) is excerpted over the water-covered area to evaluate the statistical distribution of  $r$ . Although this analysis is undertaken on the whole SAR dataset, two showcases are selected and discussed, see Fig. 1(c) and (d). The histograms of  $r$ , evaluated within the ROIs extracted from the SARs scenes depicted in Fig. 1(c) and (d), are shown in Fig. 3(a) and (b), respectively, where, for reference purposes, the Burr probability density function (pdf) [21] is also depicted in red. It can be noted that, in both cases, the empirical distribution is well approximated by the Burr pdf. This is also quantitatively confirmed by the Kolmogorov–Smirnov binary hypothesis test undertaken using a significance level equal to 0.05 [22], [23]. Accordingly, the relationship between the probability of false alarm  $P_{fa}$  and the CFAR threshold  $th$  is given by [21]

$$P_{fa} = \int_{th}^{\infty} \frac{\alpha\beta^{\alpha}\mu r^{\mu-1}}{(\beta + r^{\mu})^{\alpha+1}} dr, \quad r > 0 \quad (3)$$

where  $\alpha$  and  $\mu$  are the nonnegative shape parameters while  $\beta$  is a nonnegative scale parameter. Hence, the CFAR threshold is given by

$$th = \left( \beta \left[ P_{fa}^{-\frac{1}{\alpha}} - 1 \right] \right)^{\frac{1}{\mu}}. \quad (4)$$

When dealing with the SP metrics, the histograms of  $\sigma_{VV}^0$  and  $\sigma_{VH}^0$  are shown in Fig. 3(c)–(f), where the generalized Gamma distribution (GFD) is also depicted for reference purposes [24]. Even in this case, to quantitatively confirm the soundness of the theoretical distributions, the Kolmogorov–Smirnov binary hypothesis test is applied with a significance level equal to 0.05. Accordingly, the relationship between  $P_{fa}$  and  $th$  is given by [25]

$$P_{fa} = \int_{th}^{\infty} \frac{|\nu| \mu^{\mu}}{\sigma \Gamma(\mu)} \left( \frac{x}{\sigma} \right)^{\mu \nu - 1} e^{-\mu \left( \frac{x}{\sigma} \right)^{\nu}} dx, \quad x > 0 \quad (5)$$

where  $\Gamma(\cdot)$  is the Gamma function,  $\sigma$  and  $\mu$  represent the nonnegative scale and power parameters, respectively, and  $\nu$  is the shape parameter. Hence, the CFAR threshold is given by [25]:

$$th = \begin{cases} \sigma \left( \frac{1}{\mu} \Gamma^{-1} (1 - P_{fa}, \mu) \right)^{\frac{1}{\nu}}, & \nu > 0 \\ \sigma \left( \frac{1}{\mu} \Gamma^{-1} (P_{fa}, \mu) \right)^{\frac{1}{\nu}}, & \nu < 0 \end{cases}. \quad (6)$$

Once the binary image is obtained, the 1-pixel continuous waterline is extracted using the Sobel edge detection algorithm.

To monitor the time variability of the water-covered area, Shannon entropy is considered [26]:

$$H(x_i) = - \sum_{k=1}^N p_k(x_i) \log p_k(x_i) \quad (7)$$

where

$$p_k(x_i) = \text{Prob}(x_i = X). \quad (8)$$

$N$  is the number of the SAR scenes in the time series,  $x \in \{r, \sigma_{VV}^0, \sigma_{VH}^0\}$  and  $p_k(x_i)$  are the probability that the pixel  $i$  of the  $k^{\text{th}}$  input image  $x$  is equal to  $X$  along the whole time series. Hence, lower (higher)  $H$  values are expected to call for pixels whose values exhibit an almost constant (variable) behavior over the whole time series. This means that  $H$  can be used to estimate the time variability of the water-covered area according to the specific metric adopted.

### III. EXPERIMENTS

In this section, a time series of 29 Sentinel-1 SAR scenes collected from April 13, 2016 to May 9, 2018 over an area including the Monte Cotugno reservoir is considered to monitor the time variability of the water-covered area. All the SAR scenes are collected in DP VV/VH imaging mode, descending pass, under an incidence angle of  $\approx 40^\circ$ . In Fig. 1(c) and (d), excerpts related to two SAR scenes are depicted. By visually analyzing these images, it can be noted that the water body of the Monte Cotugno reservoir exhibits significant variations over time (the time span between the two images is about 17 months), as further witnessed by the corresponding Sentinel-2 imagery, see Fig. 1(a) and (b). Remarkable loss of water-covered areas is experienced over both the southern and northwestern parts of the reservoir, indicating a significant shrink of the waterline. The two SAR scenes of Fig. 1(c) and (d) are hereinafter considered as showcases to discuss the performance of the proposed methodology to extract the waterline and estimate the water body area. First, the water/land separability is addressed exploiting both DP and SP information; then, the waterline is extracted over the whole times

series and the time variability of the reservoir water-covered area is analyzed.

To assess the performance of the proposed metrics in separating land from water, the actual histograms of  $r$ ,  $\sigma_{VV}^0$ , and  $\sigma_{VH}^0$  are evaluated within two equal-size ROIs belonging to land and water. Hence, the Bhattacharyya distance  $D_B$  between the land and water histograms is evaluated using [27], [28]:

$$0 \leq D_B = -\ln \left( \sum_{i \in X} \sqrt{(w(i)l(i))} \right) \leq \infty. \quad (9)$$

$D_B$  allows quantifying the overlap between the histograms of the land ( $l$ ) and water ( $w$ ) samples. The lower the  $D_B$  the closer are the two distributions and, therefore, the lower is the water/land separation.  $D_B$  evaluated over the ROIs selected from the SAR scene of Fig. 1(c) are 1.81, 1.55, and 1.68 for  $r$ ,  $\sigma_{VV}^0$ , and  $\sigma_{VH}^0$ , respectively; while  $D_B$  values that refer to the SAR scene of Fig. 1(d) are 1.94, 1.48, and 1.65 for  $r$ ,  $\sigma_{VV}^0$ , and  $\sigma_{VH}^0$ , respectively. Hence, the DP approach provides the largest water/land separation, enhancing the contrast with respect to SP channels.

To generate the binary image, the global threshold CFAR approach described in Section II is applied to each metric setting  $P_{fa} = 10^{-6}$ . The binary outputs related to  $r$ ,  $\sigma_{VV}^0$ , and  $\sigma_{VH}^0$  are shown in Fig. 4(a)–(f), respectively. In all the cases, the proposed approach allows clearly identifying the water body, highlighting the significant loss of water-covered area that occurred in the Monte Cotugno reservoir from June 2016 to November 2017. However, subtle differences are observed among the SP/DP binary outputs that will be further analyzed by extracting the corresponding waterlines.

To extract the waterline, Sobel edge detector is applied. Results are shown in Fig. 5, where the waterlines extracted using  $r$ ,  $\sigma_{VV}^0$ , and  $\sigma_{VH}^0$  are superimposed to the VV-polarized NRCS SAR image. The waterlines are shown in RGB false color composite where red, green, and blue are associated with  $r$ ,  $\sigma_{VV}^0$ , and  $\sigma_{VH}^0$ , respectively. It can be noted that, in both SAR scenes, the extracted waterline mainly calls for white color, witnessing a good overlapping between waterlines extracted using DP and SP approaches. However, significant differences can be observed over the northwestern and southern parts of the reservoir, where  $\sigma_{VH}^0$  visually results in the worst performance due to the presence of several false edges. To better appreciate the differences, two zoom-in areas are depicted in Fig. 5. It can be noted that the waterline extracted from  $r$  and  $\sigma_{VV}^0$  well fits the profile of the reservoir while  $\sigma_{VH}^0$  calls for false edges that result in an overestimation of the extent of the water-covered area, see the blue waterline in Fig. 5(b).

The water-covered area is estimated from the binary imagery considering the  $10 \text{ m}^2$  pixel size. Results, obtained processing the whole time-series, are shown in Fig. 6, where the water-covered area obtained from independent ground information is also annotated for reference purposes, see dashed black curve. This ground information is provided by the “Ente per lo Sviluppo dell’Irrigazione e la Trasformazione Fondiaria in Puglia, Lucania e Irpinia” and made available from the “Autorità di Bacino della Basilicata” (AdB) at <http://www.adb.basilicata.it/adb/risorseidriche/dispoedriche/sceglida>

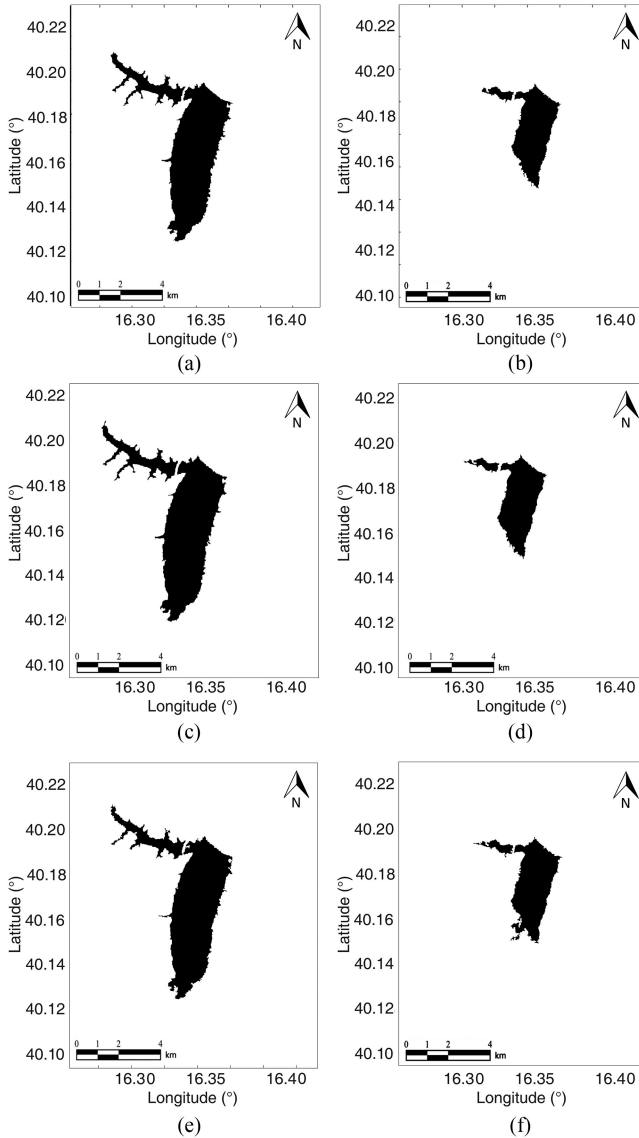


Fig. 4. Binary imagery obtained using the global threshold CFAR method with  $P_{fa} = 10^{-6}$ . The figure is organized in a matrix format where rows correspond to the different input images, i.e.,  $r$ ,  $\sigma_{VV}^0$ , and  $\sigma_{VH}^0$ , while columns refer to the different SAR scenes, i.e., the dataset collected on June 12, 2016 and November 4, 2017.

tidighe.asp). The water-covered area is obtained using a remotely controlled distributed network of sensors and actuators implemented according to the supervisory control and data acquisition (SCADA) framework. The plot of Fig. 6 clearly shows that both DP and SP metrics provide estimations of the water-covered area that well fit the reference AdB ground information, witnessing the soundness of the proposed methodology. The expected seasonal trend can be recognized very well from the extracted water-body areas and, in addition, one can also note the anomalous water loss experienced by the reservoir during the autumn/winter season of 2017. By intercomparing the accuracy of the water-covered area estimated using the different metrics with the reference AdB information, one can note that  $r$  performs best; while the worst

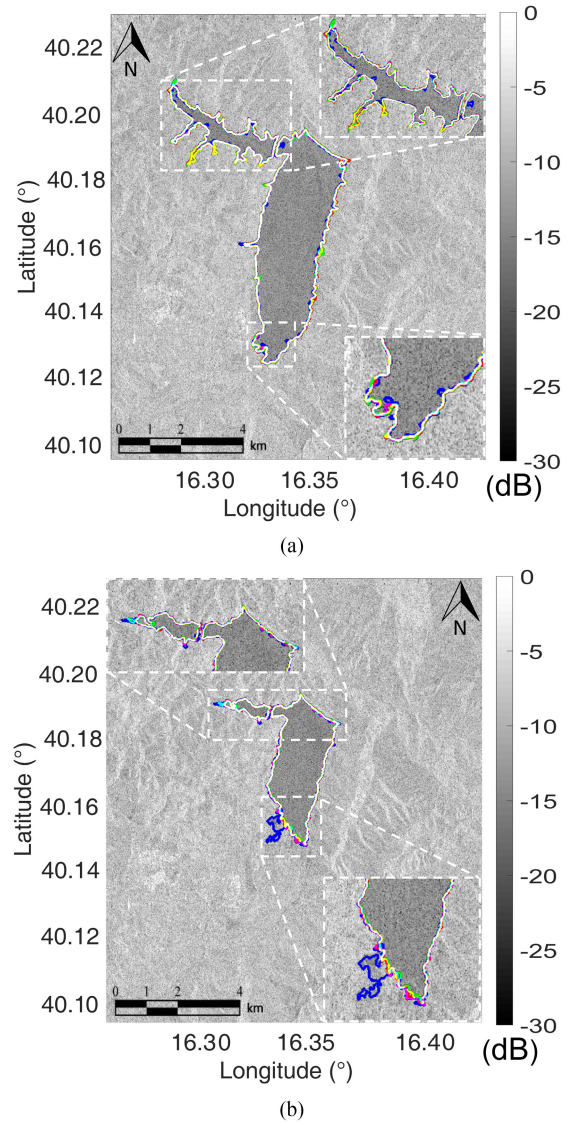


Fig. 5. Waterlines extracted from  $r$  (red),  $\sigma_{VV}^0$  (green), and  $\sigma_{VH}^0$  (blue) input images superimposed on the original VV-polarized NRCS SAR image relevant to the showcased dataset shown in Fig. 1(c) and (d). Critical areas particularly affected by waterline changes are highlighted in dashed white boxes.

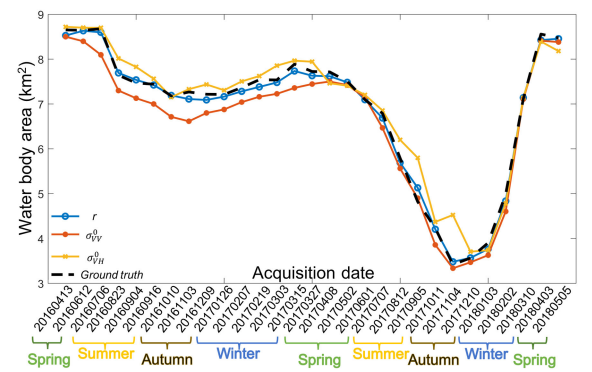


Fig. 6. Water-body area estimated along the whole time series from  $r$  (blue circles),  $\sigma_{VV}^0$  (red dots), and  $\sigma_{VH}^0$  (yellow crosses) binary imagery. The reference water-covered area provided by the AdB external source is also annotated in dashed black line.

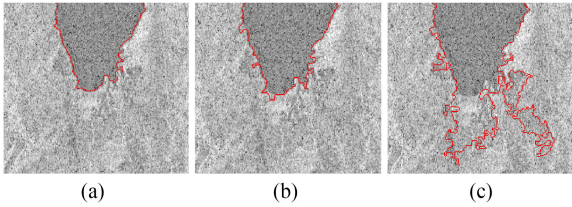


Fig. 7. Waterlines extracted from (a)  $r$ , (b)  $\sigma_{VV}^0$ , and (c)  $\sigma_{VH}^0$  images relevant to the SAR scene collected on September 5, 2017. They are superimposed on an excerpt of the VV-polarized NRCS SAR imagery.

TABLE I

MEAN AND STANDARD DEVIATION OF THE DISTANCE BETWEEN THE WATER-COVERED AREA PROVIDED BY ADB AND ESTIMATED FROM THE SAR SCENES

	Mean error ( $\text{km}^2$ )	Standard deviation error ( $\text{km}^2$ )
$r$	-0.47e-01	0.98e-01
$\sigma_{VV}^0$	-2.75e-01	1.81e-01
$\sigma_{VH}^0$	+1.37e-01	3.07e-01
FCM <sub>VV</sub>	-5.49e-01	4.54e-01
FCM <sub>VH</sub>	-6.65e-01	2.19e-01

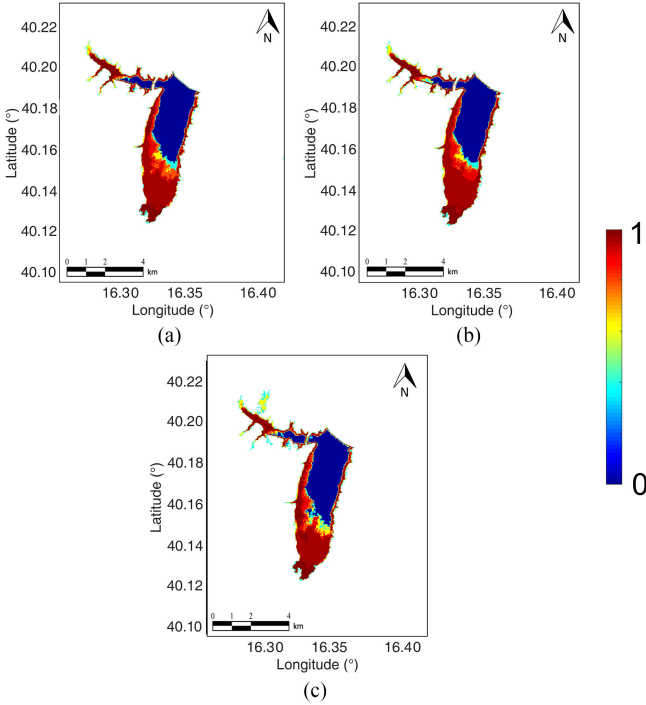


Fig. 8. Time-change rate maps based on the Shannon entropy  $H$ . Output obtained from (a)  $r$ , (b)  $\sigma_{VV}^0$ , and (c)  $\sigma_{VH}^0$ .

performance is achieved by  $\sigma_{VH}^0$  which tends to overestimate the water-covered area.

To qualitatively evaluate the performance provided by SP and DP metrics, an additional showcase is presented which is related to the SAR scene collected on September 5, 2017. An excerpt of the VV-polarized NRCS that includes the southern part of the Monte Cotugno reservoir is shown in Fig. 7 where the waterline extracted using  $r$ ,  $\sigma_{VV}^0$ , and  $\sigma_{VH}^0$  are also shown, see Fig. 7(a)–(c). By visually intercomparing the extracted waterlines, one can note that the  $\sigma_{VH}^0$  metric results in a large number of false edges

that, at once, lead to an overestimation of the water-covered area. The number of false edges decreases when the  $\sigma_{VV}^0$  metric is used while the  $r$  metric results in the best performance.

A quantitative performance analysis is also undertaken by measuring the distance between the estimated water-covered area and the reference AdB information for each SAR scene and each metric, see Table I. In addition, the metrics are also contrasted with a Fuzzy c-means clustering (FCM) that was applied in [29] to both co- and cross-polarized channels for land/sea discrimination purposes. Experimental results confirm the previous results, showing that  $r$  outperforms both  $\sigma_{VV}^0$  and  $\sigma_{VH}^0$ . In addition,  $r$  provides results better than the FCM method.

To provide an added-value map where the time variability of the water-covered area is highlighted, the Shannon entropy  $H$  [see (6)] is evaluated for  $r$ ,  $\sigma_{VV}^0$ , and  $\sigma_{VH}^0$  over the whole time series, see Fig. 8(a)–(c), respectively. Blue areas result in almost no changes ( $H \approx 0$ ) while dark red areas result in remarkable changes ( $H \approx 1$ ). It must be pointed out that, as suggested by previous experiments, the largest time-change rate occurs in the northwestern and southern parts of the reservoir, while limited changes are observed in the central and northeastern parts. This is likely due to bathymetry.

#### IV. CONCLUSION

In this article, a time series of DP VV/VH Sentinel-1 SAR imagery was exploited to support the SWM. A methodology was proposed which is based on two steps: waterline extraction and water-body area estimation. Two different metrics were analyzed for waterline extraction that relies on DP, i.e.;  $r$ , and SP, i.e.,  $\sigma_{VV}^0$  and (c)  $\sigma_{VH}^0$ , information. An analysis of the temporal/spatial variability of the water-body area is also undertaken to provide further insights on the reservoir dynamics.

Experiments, undertaken on SAR scenes related to the reservoir of Monte Cotugno (Basilicata region, Italy) showed the following.

- 1) Sentinel-1 SAR imagery can be successfully exploited to assist/complement the management of reservoirs. In fact, the proposed approach allows observing both the seasonal trend and anomalies.
- 2) DP measurements are shown to outperform SP ones in terms of accuracy of the extracted water profiles.
- 3) When focusing on SP channels, the copolarized channel provides performance better than the cross-polarized one that resulted in a large number of false waterlines.
- 4) A time-series analysis can be successfully exploited to distinguish reservoir areas, which are permanently water covered from areas whose flooding conditions vary seasonally.

#### ACKNOWLEDGMENT

The authors would like to thank the anonymous reviewers for their constructive comments and useful suggestions. The authors would also like to thank the European Space Agency for providing Sentinel-1 data and the “Autorità di Bacino della Basilicata” for providing ground information on the Monte Cotugno reservoir through their SWM system.

## REFERENCES

- [1] Y. Ye, L. Liang, H. Zhao, and Y. Jiang, "The system architecture of smart water grid for water security," *Procedia Eng.*, vol. 154, pp. 361–368, 2016.
- [2] C. Pipitone, A. Maltese, G. Dardanelli, M. Lo Brutto, and G. La Loggia, "Monitoring water surface and level of a reservoir using different remote sensing approaches and comparison with dam displacements evaluated via GNSS," *Remote Sens.*, vol. 10, no. 1, 2018, Art. no. 71.
- [3] X. Ding and X. Li, "Monitoring of the water-area variations of lake Dongting in China with ENVISAT ASAR images," *Int. J. Appl. Earth Observ. Geoinf.*, vol. 13, no. 6, pp. 894–901, 2011.
- [4] D. Molden, "Water for food, water for life: A comprehensive assessment of water management in agriculture: Summary," Int. Water Manage. Inst., IWMI Books, Reports H039769, 2007.
- [5] Y. Zhou, L. Zhang, and Y. Wang, "Monitoring of water extent and variation of the Poyang lake using GF-1 remote sensing data," in *Proc. 7th Int. Conf. Manuf. Sci. Eng.*, 2017.
- [6] W. G. Buma, S. I. Lee, and J. Y. Seo, "Recent surface water extent of lake Chad from multispectral sensors and GRACE," *Sensors*, vol. 18, no. 7, 2018, Art. no. 2082.
- [7] F. Ulaby, R. Moore, and A. Fung, *Microwave Remote Sensing: Active and Passive: Volume II*. Reading, MA, USA: Addison-Wesley, 1981.
- [8] J. Lee and I. Jurkevich, "Coastline detection and tracing in SAR images," *IEEE Trans. Geosci. Remote Sens.*, vol. 28, no. 4, pp. 662–668, Jul. 1990.
- [9] H. Liu and K. C. Jezek, "Automated extraction of coastline from satellite imagery by integrating Canny edge detection and locally adaptive thresholding methods," *Int. J. Remote Sens.*, vol. 25, no. 5, pp. 937–958, 2004.
- [10] L. Xing, X. Tang, H. Wang, W. Fan, and G. Wang, "Monitoring monthly surface water dynamics of Dongting lake using Sentinel-1 data at 10 m," *PeerJ*, vol. 6, 2018, Art. no. e4992.
- [11] J. Li and S. Wang, "An automatic method for mapping inland surface waterbodies with Radarsat-2 imagery," *Int. J. Remote Sens.*, vol. 36, no. 5, pp. 1367–1384, 2015.
- [12] L. Zeng, M. Schmitt, L. Li, and X. X. Zhu, "Analysing changes of the Poyang lake water area using Sentinel-1 synthetic aperture radar imagery," *Int. J. Remote Sens.*, vol. 38, no. 23, pp. 7041–7069, 2017.
- [13] G. Kaplan, Z. Y. Avdan, and U. Avdan, "Mapping and monitoring wetland dynamics using thermal, optical, and SAR remote sensing data," in *Wetlands Management*, D. Gke, Ed. Rijeka: IntechOpen, 2019.
- [14] M. Masetti, S. Pettinato, S. V. Nghiem, S. Paloscia, D. Pedretti, and E. Santi, "Combining COSMO-SkyMed satellites data and numerical modeling for the dynamic management of artificial recharge basins," *J. Hydrol.*, vol. 567, pp. 41–50, 2018.
- [15] A. Loperte, F. Soldovieri, and V. Lapenna, "Monte Cotugno dam monitoring by the electrical resistivity tomography," *IEEE J. Sel. Topics Appl. Earth Observ. Remote Sens.*, vol. 8, no. 11, pp. 5346–5351, Nov. 2015.
- [16] R. Maini and H. Aggarwal, "Study and comparison of various image edge detection techniques," *Int. J. Image Process.*, vol. 3, no. 1, pp. 1–11, 2009.
- [17] E. Ferrentino, F. Nunziata, and M. Migliaccio, "Full-polarimetric SAR measurements for coastline extraction and coastal area classification," *Int. J. Remote Sens.*, vol. 38, no. 23, pp. 7405–7421, 2017.
- [18] F. Nunziata, A. Buono, M. Migliaccio, and G. Benassai, "Dual-polarimetric C- and X-band SAR data for coastline extraction," *IEEE J. Sel. Topics Appl. Earth Observ. Remote Sens.*, vol. 9, no. 11, pp. 4921–4928, Nov. 2016.
- [19] D. Di Luccio *et al.*, "Shoreline rotation analysis of embayed beaches by means of in situ and remote surveys," *Sustainability*, vol. 11, no. 3, 2019, Art. no. 725.
- [20] A. M. Atto, E. Trouv, J. Nicolas, and T. T. Li, "Wavelet operators and multiplicative observation models-application to SAR image time-series analysis," *IEEE Trans. Geosci. Remote Sens.*, vol. 54, no. 11, pp. 6606–6624, Nov. 2016.
- [21] G. V. Weinberg and C. Tran, "Burr distribution for X-band maritime surveillance radar clutter," *Prog. Electromagn. Res. B*, vol. 81, pp. 183–201, 2018.
- [22] S. M. Davis *et al.*, *Remote Sensing: The Quantitative Approach*. New York, NY, USA: McGraw-Hill, 1978.
- [23] V. W. Berger and Y. Zhou, *Kolmogorov-Smirnov Test: Overview*. Atlanta, GA, USA: Amer. Cancer Soc., 2014.
- [24] J. Sun, X. Wang, X. Yuan, Q. Zhang, C. Guan, and A. V. Babanin, "The dependence of sea SAR image distribution parameters on surface wave characteristics," *Remote Sens.*, vol. 10, no. 11, 2018, Art. no. 1843.
- [25] X. Qin, S. Zhou, H. Zou, and G. Gao, "A CFAR detection algorithm for generalized Gamma distributed background in high-resolution SAR images," *IEEE Geosci. Remote Sens. Lett.*, vol. 10, no. 4, pp. 806–810, Jul. 2013.
- [26] R. Pathria and P. D. Beale, *Statistical Mechanics*, 3rd ed. New York, NY, USA: Academic, 2011.
- [27] A. Bhattacharyya, "On a measure of divergence between two multinomial populations," *Sankhy, The Indian J. Statist. (1933–1960)*, vol. 7, no. 4, pp. 401–406, 1946.
- [28] F. Nunziata, A. Buono, and M. Migliaccio, "Cosmo-SkyMed synthetic aperture radar data to observe the deepwater horizon oil spill," *Sustainability*, vol. 10, no. 10, 2018, Art. no. 3599.
- [29] M. Modava and G. Akbarzadeh, "Coastline extraction from SAR images using spatial fuzzy clustering and the active contour method," *Int. J. Remote Sens.*, vol. 38, no. 2, pp. 355–370, 2017.



**Emanuele Ferrentino** (S'16) was born in Cattolica, Italy, in 1984. He received the Ph.D. degree in information engineering from the Università degli Studi di Napoli "Parthenope," Napoli, Italy, in 2019.

He is currently a Postdoc Researcher with the Università degli Studi di Napoli "Parthenope." His research interests include electromagnetic modeling, polarimetric SAR data analysis, and remote sensing land and marine applications (earthquake damage assessment, target detection, coastline extraction, and classification).



**Ferdinando Nunziata** (S'03–M'12–SM'14) was born in Avellino, Italy, in 1982. He received the Ph.D. degree in telecommunication engineering from the Università degli Studi di Napoli "Parthenope," Napoli, Italy, in 2008.

He is currently an Associate Professor with the Università degli Studi di Napoli "Parthenope." His main research interests include applied electromagnetics, i.e., sea surface scattering, radar polarimetry, SAR sea oil slick and metallic target monitoring, spatial resolution enhancement techniques, and

GNSS-R.



**Andrea Buono** (S'14) was born in Napoli, Italy, in 1984. He received the Ph.D. degree in information engineering from the Università degli Studi di Napoli "Parthenope," Napoli, Italy, in 2017.

He is currently a Researcher with the Università degli Studi di Napoli "Parthenope." His main research interests include applied electromagnetics, including electromagnetic modeling, single- and multipolarization sea surface scattering, radar polarimetry, and SAR ocean and coastal area monitoring.



**Angelo Urciuoli** (S'14) was born in Napoli, Italy, in 1983. He is currently working toward the Ph.D. degree in information and communication technology and engineering with the Università degli Studi di Napoli "Parthenope," Napoli, Italy.

His research interests include electromagnetic modeling, polarimetric SAR data analysis, and remote sensing marine applications as coastline extraction and classification.



**Maurizio Migliaccio** (M'91–SM'00–F'17) was born in Napoli, Italy, in 1962. He received the Laurea degree (Hons.) in electronic engineering from the Università degli Studi di Napoli "Federico II," Napoli, Italy, in 1987.

He is currently a Full Professor of electromagnetics with the Università degli Studi di Napoli "Parthenope," Napoli, Italy.

His current scientific interests include remote sensing for marine and coastal applications, polarimetry, inverse problem for resolution enhancement, and reverberating chambers.